

Glassy Li Metal Anode for High-Performance Rechargeable Li Batteries

Xuefeng Wang^{1†}, Gorakh Pawar^{2†}, Yeqing Li¹, Xiaodi Ren³, Minghao Zhang¹, Bingyu Lu¹,
Abhik Banerjee¹, Ping Liu¹, Eric J. Dufek⁴, Ji-Guang Zhang³, Jie Xiao³, Jun Liu³, Ying Shirley
Meng^{1*}, Boryann Liaw^{4*}

¹ Department of NanoEngineering, University of California San Diego, 9500 Gilman Drive, La Jolla, CA 92093, USA

² Department of Material Science and Engineering, Idaho National Laboratory, 1955 N. Fremont Avenue, Idaho Falls, ID 83415, USA

³ Energy and Environmental Directorate, Pacific Northwest National Laboratory, 902 Battelle Boulevard, Richland, Washington 99354, United States

⁴ Department of Energy Storage and Advanced Vehicles, Idaho National Laboratory, 1955 N. Fremont Avenue, Idaho Falls, ID 83415, USA

* Correspondence to: boryann.liaw@inl.gov (B. Liaw); shirleymeng@ucsd.edu (Y.S. Meng)

† GP and XW are co-first authors, who made equal contributions to the major content of the article.

Abstract:

Controlling nanostructure from molecular, crystal lattice to the electrode level remains as arts in practice, where nucleation and growth of the crystals still require more fundamental understanding

and precise control to shape the microstructure of metal deposits and their properties. This is vital to achieve dendrite-free Li metal anodes with high electrochemical reversibility for practical high-energy rechargeable Li batteries. Here, cryogenic-transmission electron microscopy was used to capture the dynamic growth and atomic structure of Li metal deposits at the early nucleation stage, in which a phase transition from amorphous, disordered states to a crystalline, ordered one was revealed as a function of current density and deposition time. The real-time atomic interaction over wide spatial and temporal scales was depicted by the reactive-molecular dynamics simulations. The results show that the condensation accompanied with the amorphous-to-crystalline phase transition requires sufficient exergy, mobility and time to carry out, contrary to what the classical nucleation theory predicts. These variabilities give rise to different kinetic pathways and temporal evolutions, resulting in various degrees of order and disorder nanostructure in nano-sized domains that dominate in the morphological evolution and reversibility of Li metal electrode. Compared to crystalline Li, amorphous/glassy Li outperforms in cycle life in high-energy rechargeable batteries and is the desired structure to achieve high kinetic stability for long cycle life.

Main Text:

Metal based anodes, such as lithium (Li) metal can lead to the highest energy density for rechargeable batteries, and show great promise to meet the increasing energy demand for all kinds of applications in the future. However, most Li metal electrodes suffer from poor electrochemical reversibility, which not only reduce the capacity and cycle life but also increase the operational safety concern. Since the properties of the Li metals (e.g. nano-/microstructure, surface morphology and electrochemical performance) in the rechargeable batteries are largely governed by the electrochemical process, it is critical to comprehend the underlying mechanism of Li deposition by both experimental and theoretical work, especially in the very early stage of

nucleation to seek better control of the Li deposition. This understanding is also vital to the formation of other functional materials, such as metallic glasses.

To explore the behavior of metals during electrodeposition, various experimental techniques have been developed to capture the kinetic growing and probe the structural evolution at different stages and conditions. Take Li metal as an example, **Fig. 1** and Table S1 display most of the useful tools dedicated to Li metal study at a wide range of detective spatial scale with their main achievements. It is worth noting that majority of them is capable of probing the microstructure of the Li metal, which shows a variety of morphologies (ranging from sheets to whiskers) depending on the applied current density, electrolyte composition and additional experimental conditions. Although *in situ*, *operando* microscopies allow to visualize the real-time microstructure evolution ^{1, 2, 3, 4, 5, 6, 7}, it is still very difficult to capture the initial stage of Li deposition when Li metal begins to nucleate and subsequently grow into stable microstructures. In order to push the detection limit to nano or even atomic scale, cryogenic protection is essential to minimize the beam damage, while preserving the intrinsic property and microstructure of Li deposits. Recently, the cryogenic-electron microscopy (cryo-EM) has been proved useful to study the nanostructures of Li metal and reveal the variations in its crystallinity and the structure of the solid electrolyte interphases (SEI) ^{8, 9}. Such variations may significantly alter the growth of Li deposits and their physicochemical properties, and such an understanding has not been established before. A thorough understanding of the evolution of these variations at the early stage is thus vital to precisely control the nano-/microstructure of the electrodeposited Li metal and enable a high-performance anode for rechargeable Li batteries.

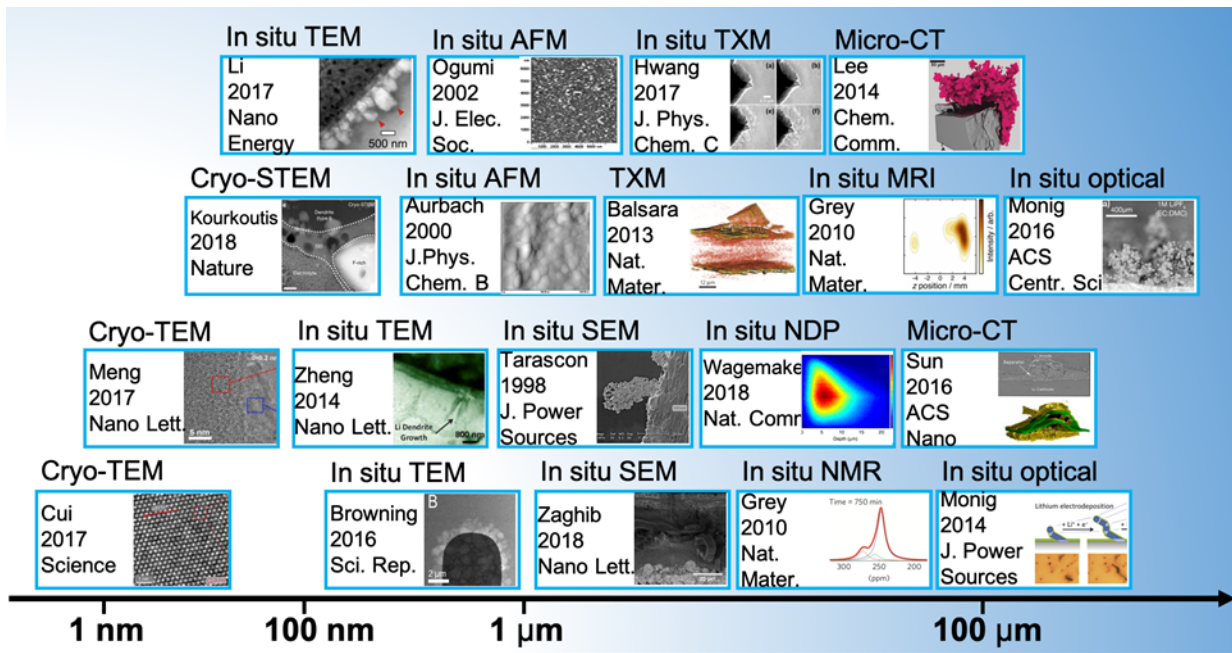


Fig. 1. Summarized experimental effort on exploring the growth mechanism of Li by different methods in a wide range of scale and resolution in the observation.

The classical nucleation theory depicts that nuclei would appear if the embryo's bulk Gibbs energy overcomes the surface energy and grow when the size of embryo exceeds the critical radius ¹⁰. For electrochemical nucleation, this process is driven by the charge transfer of ions neutralized with electrons and sustained by the mass transport of ions near the electrolyte-electrode interface ¹¹. Based on these principles, several models have been proposed to illustrate the mechanisms and kinetics of electrochemical phase formation in the initial nucleation stages, such as phase field model ¹², heterogeneous nucleation model ¹³, surface nucleation and diffusion model ^{14, 15}, space-charge model ¹⁶, and Li/SEI growth model ⁷. These models underline some key contributions like free energy, surface tension and overpotential, which are macroscopic properties determined by the experiments but become ambiguous when dealing with a nucleus that only comprises a few atoms. These properties also do not describe the atomic interactions,

attachment and detachment kinetics to small clusters with sufficient details to delineate different nanostructure configurations, which is urgently required to develop microscopic and even atomistic models to understand the Li nucleation and growth.

Herein, we applied cryogenic-transmission electron microscopy (cryo-TEM) to capture the kinetic progression of nucleation of Li metal and use reactive-molecular dynamics (*r*-MD) simulations to understand the atomic interaction inside. The cryo-TEM imaging revealed that a phase transition from amorphous, disordered states to a crystalline, ordered one occurs as a function of current density and deposition time. The fact that amorphous or glassy Li deposits can be obtained at room temperature with very slow deposition rates (e.g. 0.1 mA cm^{-2}) is in stark contrast to conventional wisdoms that believe only possible with extreme conditions such as very high quenching rates (e.g. $>10^6 \text{ K s}^{-1}$)¹⁷. The *r*-MD simulations provide the explanation regarding kinetic pathways for nucleation and the associated amorphous-to-crystalline (disorder-to-order or second-order) phase transition. We found that the incubation time for the condensation and phase transition varies with canonical ensemble size (*S*), as well as mass and energy transfer rates between the ensemble and the neighboring environment. On this basis, the crystallinity of nuclei was correlated with the subsequent growth of the nanostructure and morphology that are pertinent to the electrochemical performance of the Li metal electrode. For instance, the amorphous or glassy Li nanostructure is beneficial to form columnar Li metal grains with high coulombic efficiency (CE), which could be controlled by several synthesis strategies including the electrolyte design. These findings not only deepen the understanding of the Li deposition kinetics and mechanisms at the atomic scale but also enlighten the possibility to

control the nano-/microstructure of the electrochemically deposited Li (EDLi) to enable high-performance rechargeable Li batteries.

Cryo-TEM Observations

The cryo-TEM results (Fig. 2 and Fig. S1¹⁸–Fig. S9) show the nano- and microstructure evolution of EDLi as a function of deposition time (5–20 min, Fig. S3 and Fig. S4) and current density (0.1–2.5 mA cm⁻², Fig. S7). At 0.5 mA cm⁻², although the deposition time was as short as 5 min, tubular EDLi was formed about 200 nm in diameter and >1 μm in length (Fig. S3). Interestingly, no lattice fringes (Fig. 2A and Fig. S4A-D), nor characteristic bright diffraction spots/rings of the body-centered cubic (*bcc*) Li metal packing in the Fast Fourier transformed (FFT) image (Fig. 2D) were found, suggesting that the EDLi is amorphous or glassy. The local structure in Fig. 2A also displays the disordered arrangement of Li atoms (comparison to those in Fig. 2C). The metallic nature of EDLi is confirmed by the electron energy loss spectrum (EELS) in Fig. S5 and electrochemical reversibility (Fig. S6)¹⁹. At 10 min, a small portion of EDLi near the surface became crystalline (Fig. 2B and Fig. S4E-H) as evident by the characteristic bright diffraction spots (labeled by the white circles) in Fig. 2E with weak contrast. Lattice fringes were present in this region (Fig. 2B) and the distance between the adjacent fringes was measured to be 0.246 nm, which corresponds to the spacing between Li (110) planes. It is worth noting that the domain of the crystalline EDLi (shown by the white dash line) is about 5 nm in size, a size the *r*-MD simulation predicted the transition to the crystalline phase is eminent and spontaneous. The degree of crystallinity of the EDLi is further enhanced with increased deposition time. For 20 min, large crystalline domains (>50 nm) and intense characteristic bright diffraction spots of the *bcc* structure were present (Fig. 2C, F, and Fig. S4I-L). Thus, at the same deposition rate, as the

deposition time increases more Li atoms aggregate to form larger embryos. Once an embryo is larger than a critical size, the amorphous-crystalline phase transition occurs.

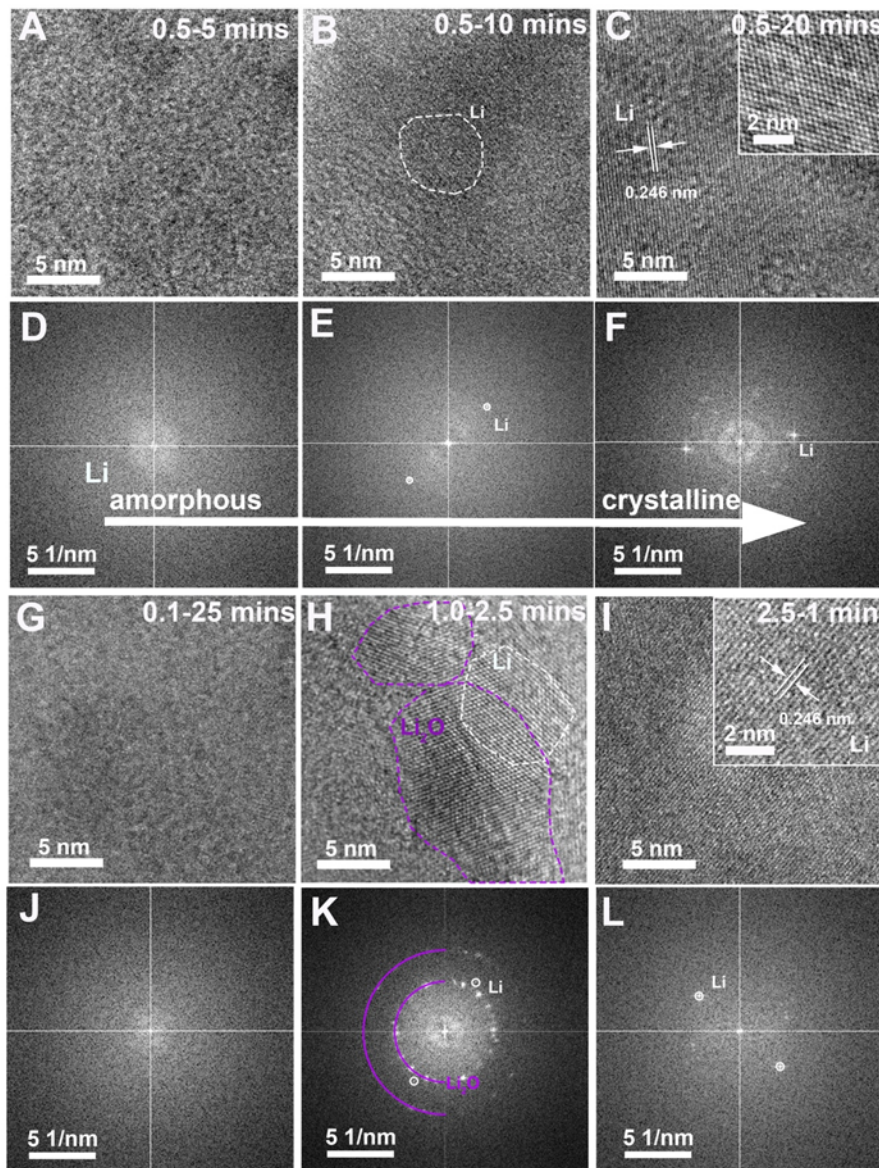


Fig. 2. Nanostructure evolution of Li deposit as a function of deposition time and current density. TEM images (A-C and G-I) and their corresponding FFT patterns (D-F and J-L) of the Li deposits at 0.5 mA cm^{-2} for 5 min (A and D), 10 min (B and E) and 20 min (C and F), 0.1 mA cm^{-2} for 25 min (G and J), 1.0 mA cm^{-2} for 2.5 min (H and K) and 2.5 mA cm^{-2} for 1.0 min (I and L).

Further studies of the nano- and microstructure dependence on current density (Fig. 2G-L for constant capacity and Fig. S7), we found that the higher the current density was used, the larger the embryo size and the higher the degree of crystallinity in EDLi (the statistical analysis is shown in Fig. S8). The EDLi is mostly amorphous at 0.1 mA cm^{-2} (Fig. 2G, J, and Fig. S7A, E, I, and M), partly crystalline at 1.0 mA cm^{-2} (Fig. 2H, K, and Fig. S7C, G, K, and O) and highly crystalline at 2.5 mA cm^{-2} (Fig. 2I, L, and Fig. S7D, H, L, and P). The crystalline domains of EDLi at 1.0 mA cm^{-2} were found near the surface (labeled by the red square in Fig. S7C) and about 5 nm in size (labeled by the white dash line in Fig. 2H), which is similar to the EDLi at 0.5 mA cm^{-2} for 10 min (Fig. 2B). These results suggest the following: (1) the embryo size is key to the second order phase transition, (2) matured crystallites are often larger than 5 nm, and (3) the embryo size is sensitive to the current density. Thus, the high current densities expedite the Li aggregation to precipitate the crystalline nuclei. This result implies the diverse local current density may lead to a wider distribution of Li embryo sizes with different degrees of crystallinity and domain sizes, as shown in Fig. S3C and F. In contrast, at 0.1 mA cm^{-2} (Fig. S3A and D).

Obtaining amorphous or glassy EDLi at low current densities is a surprising and counter-intuitive result²⁰ because it is often considered to require extreme processing conditions (e.g. extremely fast quenching rates) to produce amorphous metals. At lower current densities, as the conditions are less polarized and supposedly closer to equilibrium, a stable crystalline phase would be expected.

Reactive Molecular Dynamics Simulations

To understand this peculiar amorphous nature of the EDLi, a three-stage *r*-MD protocol was used to simulate the nucleation process with a variety of discrete canonical ensembles and conditions typically comprising (1) heating at 500 K for 0.1 ns to provide sufficient driving force for the nucleation, (2) quenching to 300 K with a cooling rate of 1 K ps⁻¹, and (3) equilibrating at 300 K for 5 ns (Fig. 3A). The reactive force field ReaxFF potential²¹ was used to simulate the Li-Li interactions and LAMMPS package^{22, 23} to perform all simulations (Fig. S10-14)^{24, 25, 26, 27, 28}. It is worth mentioning that in the heating and quenching stage, the nucleation sites dynamically evolved into more stable embryos, as Ostwald ripening explains (Fig. 3A)²⁹. Such a condensation process requires a specific “incubation time” to give the birth of a stable embryo, which is overlooked by the quasi-equilibrium models including the classical nucleation theory or density function theory to date. Intriguingly, all embryos studied here were disordered at the end of quenching, far away from the stable, ordered crystalline state. Thus, the incubation and condensation process is key to dictating the time to reach a stable lattice structure, depending on the ensemble size and the initial energy state given (Fig. 3B-D and Fig. S10).

Fig. 3B illustrates a sampling of the lattice structure of Li embryos as a function of embryo size at the end of the simulation. Lithium embryos with >700 Li atoms in the ensemble (at a packing density of $\rho = 0.0534 \text{ g cm}^{-3}$) are able to transform into a nucleus with the *bcc* lattice structure, whereas those <700 Li atoms remain disorder/amorphous. Embryos of 700 Li atoms exhibit either amorphous or crystalline states with a broad range of kinetic pathways and incubation time (Fig. 3C). Thus, embryo of 700 Li atoms, a size about 2-3 nm, sets the threshold for the amorphous-to-crystalline phase transition. Increasing the current density yields larger embryo size, which rapidly reduce the incubation time for this secondary phase transition (Fig. 3C) and

increase the fraction of *bcc* ordered/crystalline Li in the lattice (Fig. 3D). If the current density is lower than a threshold, the incubation time for the phase transition is on the order of *ns*; such long incubation time at low current densities to yield the crystalline phase is rarely emphasized by the classical nucleation theory^{30, 31}.

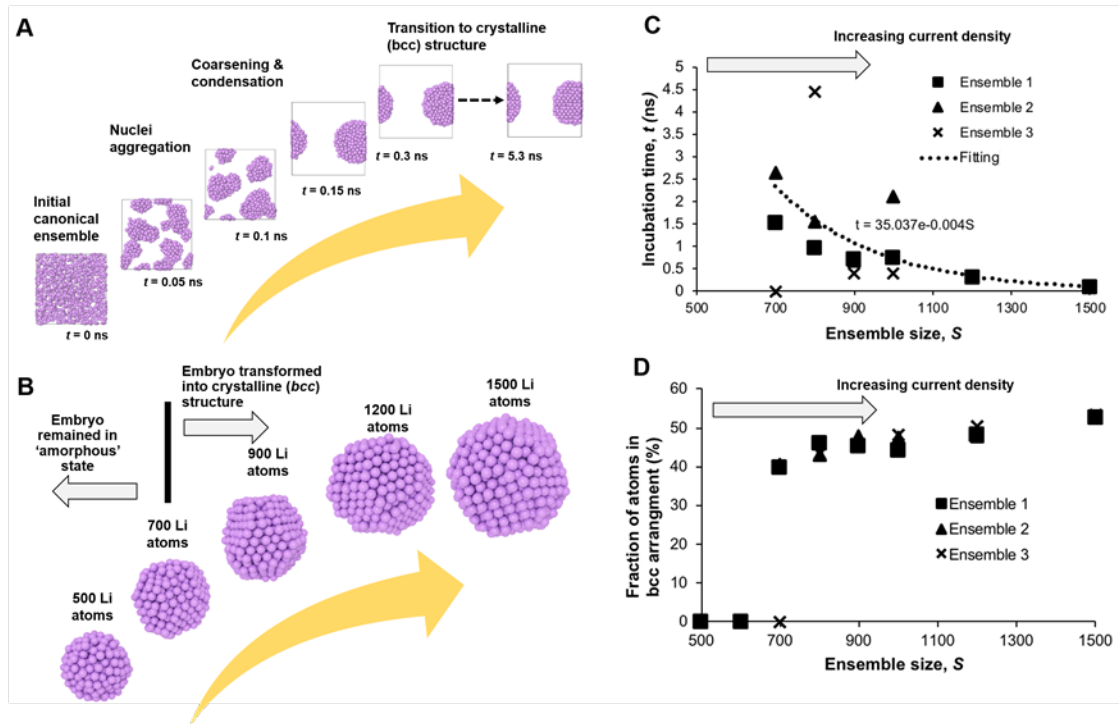


Fig. 3. MD simulation of the nucleation process of Li metal. (A) An example of the Li nucleation, growth and kinetic pathway to an embryo with an ensemble of 700 Li atoms. (B) A sampling of the final state of various sizes of embryos at the end of the simulation (5.3 ns). (C) Incubation time to second order phase transition as a function of ensemble size. (D) A fraction of Li atoms in bcc lattice arrangement as a function of ensemble size.

As Li aggregates, the incubation and physical spatial confinement from the neighbouring bodies shall determine if an embryo has sufficient exergy (primarily entropy), mobility and time to carry out the disorder-order transition. Fig. S11 illustrates the variability in the kinetic pathways and temporal nanostructure evolutions in terms of packing density, mass and energy exchange. At a

low packing density of 0.0534 g cm^{-3} (Fig. S11A), whether mass or energy exchange was confined or not, the Li aggregation produces mostly amorphous phases. As the current density increases, the packing density of Li atoms shall increase in proportion (Fig. S11B-D and Fig. S8). Further confinement in mass and energy exchange shall expedite the phase transition and shorten the incubation time. Diverse kinetic results shall determine the microstructure and morphological evolutions: from spherical amorphous nanostructures of a random distribution of sizes to a host of microstructures of diverse crystallinity, including sheets and rods that comprise amorphous nanostructures (Fig. S11A and amorphous part of Fig. S11B), mixtures of crystalline nanostructures of various sizes and shapes (crystalline part of Fig. S11B and C), and connected networks of micro-grains and micro-pores (Fig. S11D). Such a dynamic range of atomic lattice arrangements further affects the subsequent larger size microstructure evolutions, crystallinity, and morphological and shape changes in a solid particle. A larger scale (in the 100 nm) of simulation and representation of this behavior is shown in Fig. S14. On the other hand, manipulating the mass and energy exchange is able to control the size and property of the Li deposits in order to achieve high-performance application.

From Nucleation to Growth

The microstructure and morphology of the Li deposited to 1 mAh cm^{-2} loading were examined by SEM and cryo-TEM. The results are shown in Fig. 4 and found consistent with the simulation predication. Most of the Li metals grown at 0.1 mA cm^{-2} have sheet-like morphology and their planar size can be as large as several micrometers (Fig. 4A, D and G). This large sheet is originated from the amorphous nature of the Li nuclei, which mostly remained at the end of the growth (Fig. 4J). In contrast, the Li metals grown at 0.5 and 2.5 mA cm^{-2} contain about 30%

(Fig. 4K) and 80% (Fig. 4L) crystalline fragments respectively, of which the distribution is highlighted in the gold color. The crystalline Li (c-Li) fragment at 0.5 mA cm^{-2} is sandwiched between the surface SEI and the amorphous bulk Li (a-Li) (Fig. 4K), while the c-Li dominates the Li deposits at 2.5 mA cm^{-2} (Fig. 4L). As a result, ribbon- and even dendrite-like Li deposits are formed at 0.5 (Fig. 4B, E and H) and 2.5 mA cm^{-2} (Fig. 4C, F and I) with rapidly reduced planar diameter. Thus, it is reasonable to correlate the microstructure and morphology of Li deposits with the order-disorder nanostructure of the Li nuclei: the higher the crystallinity, the finer the final shape. The initial nucleation shapes the subsequent growth of the Li metal deposits.

Strategies and Applications

For a practical rechargeable Li battery, dense Li deposits with high electrochemical reversibility are highly demanded to achieve approaching 100% utilization of active Li, confine the infinite volume expansion and reduce the safety hazard caused by the Li dendrite and dead Li^{32, 33}. In this regard, glassy Li deposits are preferred and outperform the crystalline counterpart not only because of forming large size of Li deposits (Fig. 4) but also due to its higher Coulombic efficiency (CE), as evidenced in Fig. S6. The average CE at 0.1 and 0.5 mA cm^{-2} in the first 100 cycles is 95.0% and 91.5%. In contrast, at 2.5 mA cm^{-2} , the CE is unstable and drops below to 50% in the first 20 cycles. Therefore, glassy Li metal is also beneficial to enhance the electrochemical reversibility of the Li metal electrode.

For the well-known metallic glasses, the absence of the ordered nanostructure, grain boundaries and crystal defects endows them many interesting and unique properties, such as high mechanical strength, high elastic modulus, and biocompatibility³⁴. As a new member of metallic

glasses, the distinctive properties of glassy Li metal are waiting to be explored. Herein, the benefits of glassy Li metal as a rechargeable Li battery anode are illustrated in Fig. 5. The glassy nature (absence of the ordered nanostructure, grain boundaries and crystal defects) of Li metal avoids the epitaxial growth and enables the multi-dimensional growth into large grains, which is the desired form for a practical Li metal anode. The Li grains have the higher density, lower porosity and tortuosity, less reactivity and better microstructure interconnections than the dendrites. These features can significantly minimize the volume expansion, reduce the side reaction between Li and electrolyte, and maintain an effective electronic and ionic network or percolation pathway. As a consequence, a higher electrochemical reversibility would be expected for glassy Li. Therefore, from a structural perspective, glassy Li metal may be the key to solve the long-standing cyclability issue of Li metal electrode for high-energy rechargeable Li batteries.

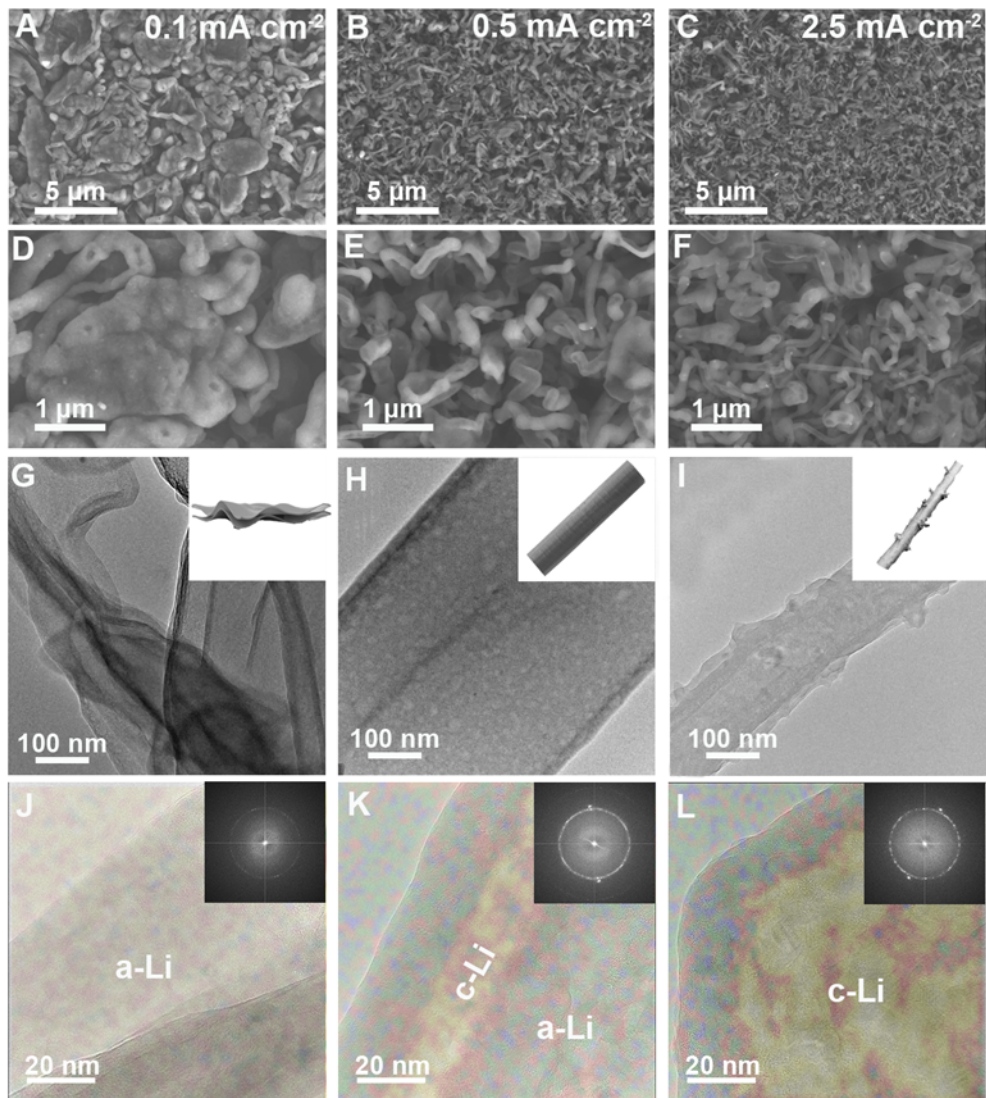


Fig. 4. Microstructure and morphology of Li deposits after 1 mAh cm^{-2} plating. SEM (A-F) and cryo-TEM images (G-L) of the Li deposits at 0.1 mA cm^{-2} for 10 hours (A, D, G and J), 0.5 mA cm^{-2} for 2 hours (B, E, H and K), and 2.5 mA cm^{-2} for 0.4 hours (C, F, I and L).

As demonstrated above, the amorphous-to-crystalline phase transition is regulated by the packing density, energy and mass transfer during nucleation process, which in turn provide the ways to facilitate the formation of favorable glassy Li metal. Reducing the current density down to the critical point will directly decrease the initial packing density and facilitate a longer incubation to

form disorder structure. An alternative way is to use the three-dimensional (3D) substrate (current collector) to reduce the effective local current density. Meanwhile, fast ion and electron conduction is advantageous for minimizing the mass and energy transfer during nucleation and growth process, which requires electrolyte design and interphase engineering. These strategies have been proved effective to obtain larger grains of Li with enhanced reversibility, although prior art has not been able to correlate the intrinsic nature of amorphous or glassy Li with the improved performance. Herein, we provide a microscopic perspective on the working principle of these strategies and propose that they could actually alter the nano- and microstructure of the Li deposits.

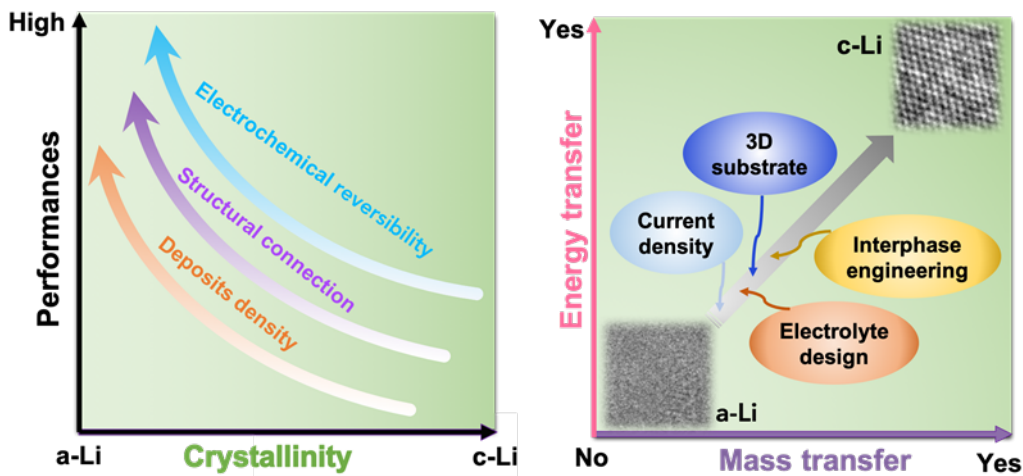


Fig. 5. Correlation between crystallinity of Li metal and performance (left) and strategies (right) to achieve better performance.

As a proof of concept, Fig. 6 shows that the electrolyte design indeed have dramatic influence on the bulk lattice structure (Fig. 6C-E) of the Li deposits during nucleation and growth, which in turn regulates the final morphology (Fig. 6A and B) and electrochemical performance (Fig. 6F). Statistical analysis results (Fig. 6C) indicate that the advanced electrolyte is in favor of forming

amorphous Li deposits (~76.8% a-Li *vs.* 23.2% c-Li), while the crystalline ones (~48.4% a-Li *vs.* 52.6% a-Li) are dominant in the baseline electrolyte. For their nanostructure, the lattice structure is predominant disorder in the former (Fig. 6E), but a mixture of order and disorder segments appeared in the latter (Fig. 6D); whereas both display similar surface SEI structure (~10 nm thick and composed of Li₂O nanocrystals; black regime). This result demonstrates that it is the intrinsic nanostructure property of Li that governed the final shape and performance of the Li metal anode. As a result, long and thin ribbon-like Li deposits (Fig. 6A) were formed in the baseline electrolyte while large Li chunky deposits found in the advanced electrolyte (Fig. 6B). Their electrochemical performance was compared by using Cu||NMC-333 cells. A Li-free anode cell configuration with only Li source comes from the cathode was used in the experiments, which is the ideal construction to achieve the highest energy-density batteries. Under this harsh condition, the cycle life of the cell is mainly dominated by the reversibility of the Li anode. As shown in Fig. 6F, the cell with baseline electrolyte fails (where the capacity drops to 0 mAh g⁻¹ based on the weight of NMC-333) quickly within five cycles. By contrast, the advanced electrolyte-based cell lasted for more than 50 cycles with a capacity retention of 59.2%, higher than any state-of-the-art reports (Table S2). This result further proves that the glassy Li metal is beneficial to achieve the best electrochemical performance for high-energy rechargeable Li batteries.

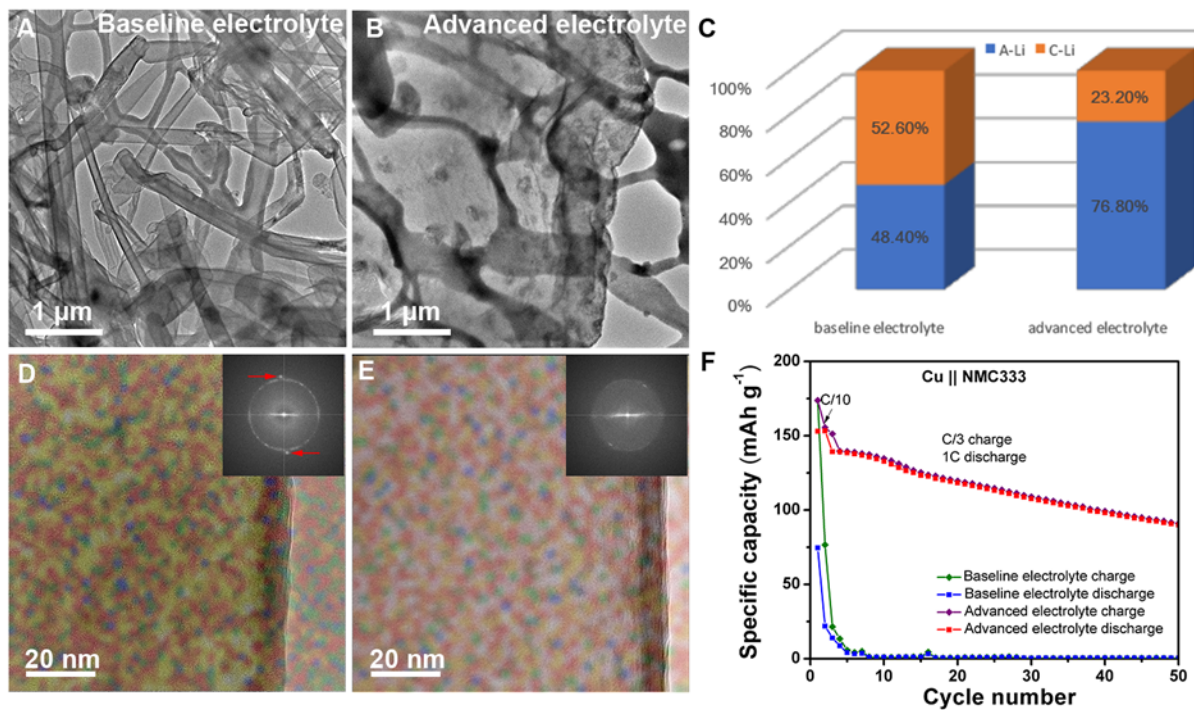


Fig. 6. The influence of electrolyte on the nano and micro structure of Li deposits and the resultant performance. Nano (D and E) and microstructure (A and B) of Li deposits from baseline electrolyte (A and D) and advanced electrolyte (B and E); statistic distribution (C) of amorphous Li (a-Li) and crystalline Li (c-Li) in two electrolytes; the cycling performance comparison (F) of two electrolytes by using Li-free anode Cu||NMC-333 cells.

Discussion

A combination of the cryogenic microscopic observations and molecular level simulations presents an explicit picture of dynamic structural and morphological changes of Li deposits from the atomic scale to a microscale particle for the first time. Depending on the atomic interaction during the initial nucleation (e.g. packing density, mass and energy transfer), the nanostructure of Li nuclei can vary from disorder to order, which eventually shape the final microstructure and affect the performance. These results from the electrochemical deposition of Li are quite different from those nucleated from vapor or liquid phase condensation as described in the

contemporary nucleation theory (CNT) based on statistical thermodynamics, of which the nucleation rate is independent of time and threshold size^{30, 31, 35}. In contrast, by tracking the real-time atomic interaction over wide spatial and temporal scales rather than averaging them as used in the CNT, our *r*-MD results suggest that the condensation process (from initial nucleation to a matured embryo) requires sufficient exergy (primarily entropy), mobility and time to carry out. This is indeed dependent of nucleation rate, incubation time and physical spatial confinement from the neighbouring bodies. These variabilities give rise to different kinetic pathways and temporal evolutions, resulting in diverse degrees of order/disorder nanostructures and their dominance in shaping the morphology, defect formation and performance of the Li metal electrode. To further illustrate this aspect, Fig. 7 provides an interesting simulation how deposition rate affects the morphology evolutions and kinetic variations in shaping the surface landscape and defect formation in the bulk. At a higher rate (Fig. 7A), less incubation time could afford a more stabilized growth of c-Li in the EDLi to create larger domains and microstructure, resulting in rougher surface and a significant amount of defect formation from dislocations, voids to grain boundaries. As the Li deposition rate decreases, smoother surface and less defects in the bulk developed in the microstructure and morphology.

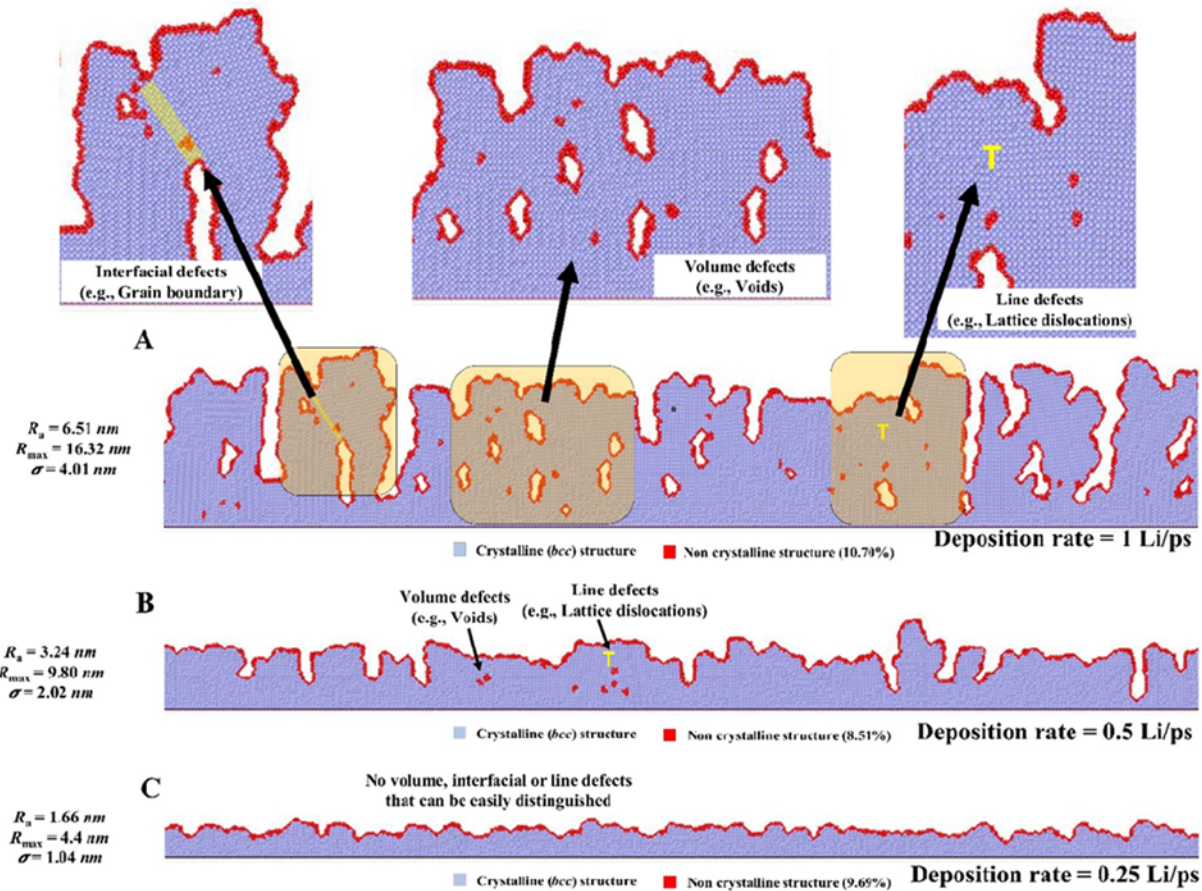


Fig. 7. Simulated results of a Li deposition at three different rates: 1 Li ps^{-1} , 0.5 Li ps^{-1} , and 0.25 Li ps^{-1} .

For rechargeable Li batteries, glassy Li has been proved to possess the desired nanostructure since it facilitates the formation of large Li grains and achieve high Coulombic efficiency. The absence of the order nanostructure and grain boundaries enables Li metal to grow along multi-dimensions rather than the epitaxial manner, and maintain good structural connection and reversibility during plating and stripping. Tuning the temporal and spatial confinements in mass and energy transfer by different strategies could help to obtain glassy Li metal deposits. These strategies could include methods to lower current density, design advanced electrolyte composition and use 3D current collector. These strategies are able to alter the bulk

microstructure of Li metal electrode and obtain chunky Li grain structures with improved cycling performance.

Amorphous metals or metallic glasses are attractive as a class of advanced functional materials for applications in different technological areas and the scientific explorations on the glass formation and glassy phenomena need more attention^{17, 20, 34, 36}. Conventional metallic glasses are made by alloying more than two metals especially transition metals by fast quenching (e.g. $>10^6 \text{ K s}^{-1}$)¹⁷. No one before us has succeeded in synthesizing metallic glasses with a single component and with very reactive alkali metals. This work demonstrates that electrochemical deposition is a powerful and effective method to obtain such amorphous metals. More importantly, the properties of such amorphous metals, amounts, and particle sizes and distributions could be tuned by adjusting the current density and deposition time through optimization. These new amorphous active metals will definitely open new opportunities to various applications besides the metallic glasses and energy storage fields, including biomedicine, nanotechnology, and microelectromechanical systems.

This amorphous-crystalline phase transition is common in many other electrochemically deposited metals, including Na, K, Mg and Zn (Fig. S15-18). As shown in Fig. 8 and Fig. S16, amorphous Na, K and Zn metals were obtained at 0.1 mA cm^{-2} for 25 min since none of their characteristic lattice structure is present in their nanostructures (Fig. 8A-D) and the corresponding FFT patterns (Fig. 8E-H). A small portion of the deposit became crystalline (Fig. 8I, J, L, M, N, and P) when the current density is increased to 0.5 mA cm^{-2} . The ordered structures of the Na, K, and Zn metals are highlighted in Fig. 8I, J, and L, respectively, which match well with the metallic Na (*bcc*), K (*bcc*) and Zn (*hcp*) lattice structure. Similar results were found in Mg, although Mg seems to yield the crystalline phase more easily than other metals.

Part of the Mg deposit is crystalline at 0.1 mA cm^{-2} for 25 min (Fig. 8K and O) while it is nearly amorphous at 0.05 mA cm^{-2} for 10 min (Fig. 8C and G). We should note that the observation of Mg in amorphous phase at the low deposition rate and short duration is of great surprise. It is because theoretical calculations suggest that it is difficult to obtain amorphous phases in the *fcc* lattice structure^{37, 38}. It is also worth noting that all the metals have a similar size of crystalline domains (labeled by the white dash line in Fig. 8I-L), which is on the order of 2-5 nm. These results suggest that these metals follow a similar nucleation mechanism during electrochemical plating. The metallic nature of these deposits is confirmed by reversible stripping (Fig. S17) and EELS spectra (Fig. S18). The r-MD simulations showed broad relevance in explaining and understanding such a common theme in nucleation and second-order phase transition phenomena.

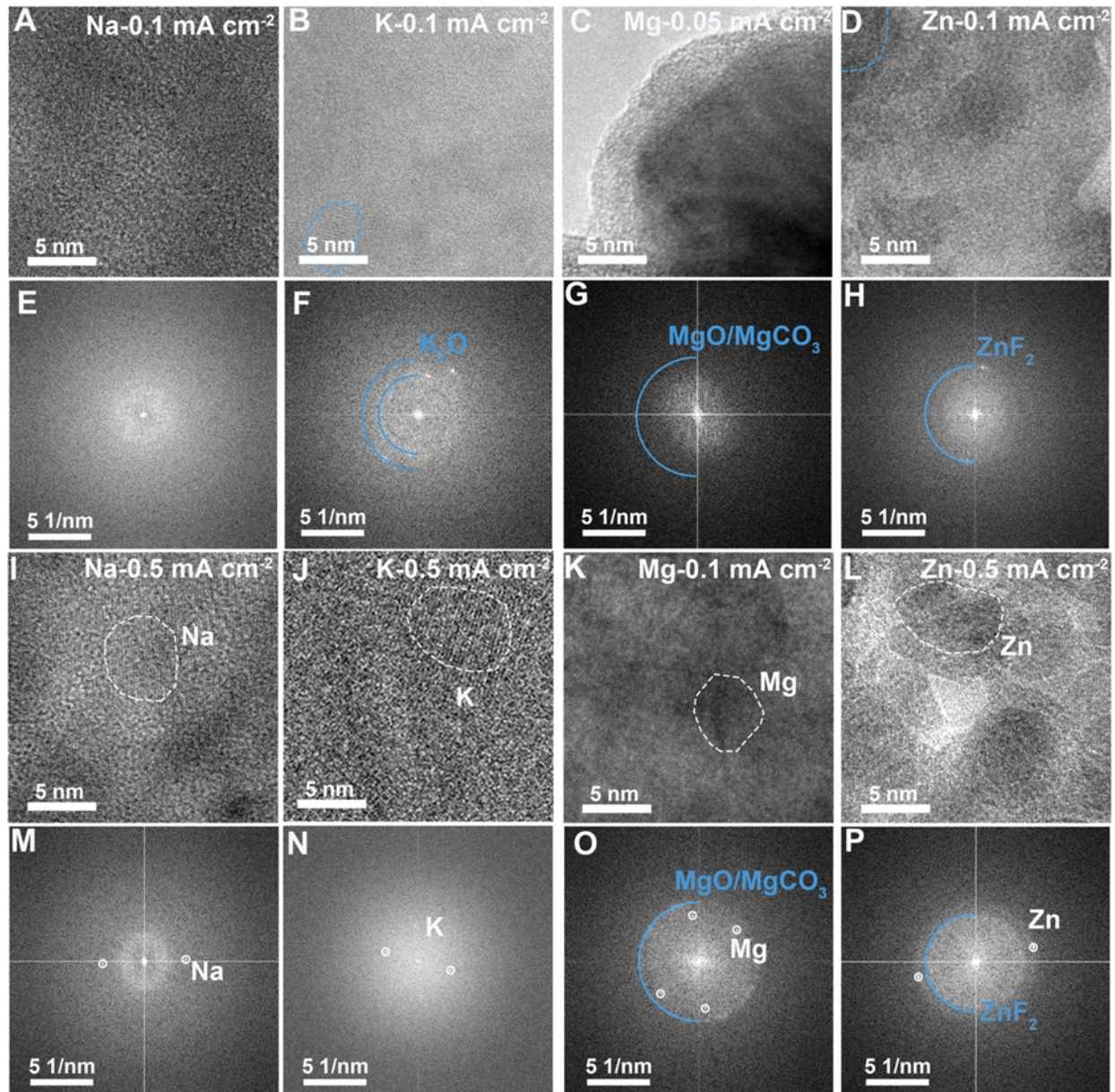


Fig. 8. Nanostructure evolution of Na, K, Mg and Zn deposits as a function of current density. TEM images (A-D and I-L) and the corresponding FFT patterns (E-H and M-P) of Na at 0.1 mA cm^{-2} (A and E) and 0.5 mA cm^{-2} (I and M), K at 0.1 mA cm^{-2} (B and F) and 0.5 mA cm^{-2} (J and N), Mg at 0.05 mA cm^{-2} (C and G) and 0.1 mA cm^{-2} (K and O) and Zn at 0.1 mA cm^{-2} (D and H) and 0.5 mA cm^{-2} (L and P). The crystalline portion of the Na, K, Mg and Zn deposits are labeled by the white dash lines.

Conclusion

From careful cryo-TEM observations and *r*-MD simulations, as we deviated from the classical nucleation theory and statistical volume- and time-averaging approach, we gained much insight into a truthful understanding of the nucleation process of metal deposition in the kinetic regime. A phase transition from amorphous, disordered states to a crystalline, ordered one occurs during electrochemical deposition, which is a function of current density and deposition time. The *r*-MD simulations indicate that the condensation process (from initial nucleation to a matured embryo) requires sufficient exergy, mobility and time to carry out, which give rise to different kinetic pathways and temporal evolutions, resulting in different degree of order/disorder nanostructure and their dominations in shaping the morphology and performance of Li metal electrode. Both experimental and computational results suggest that the critical size for amorphous-to-crystalline transition is around 2-3 nm. Compared with crystalline Li, glassy nuclei are more beneficial to form columnar Li deposits and achieve higher electrochemical reversibility for rechargeable Li batteries, which can be tuned by different control strategies, such as advanced electrolyte design. These findings not only deepen the understanding of mechanisms and kinetics of electrodeposition especially at the atomic scale, but also enlighten the potential of regulating and controlling the nano- and microstructure of metal electrodeposits to achieve high-performance for many other practical applications.

References and Notes:

1. Steiger J, Kramer D, Mönig R. Mechanisms of dendritic growth investigated by in situ light microscopy during electrodeposition and dissolution of lithium. *J Power Sources* 2014, **261**: 112-119.
2. Wood KN, Kazyak E, Chadwick AF, Chen K-H, Zhang J-G, Thornton K, *et al.* Dendrites and Pits: Untangling the Complex Behavior of Lithium Metal Anodes through Operando Video Microscopy. *ACS Central Science* 2016, **2**(11): 790-801.
3. Cohen YS, Cohen Y, Aurbach D. Micromorphological Studies of Lithium Electrodes in Alkyl Carbonate Solutions Using in Situ Atomic Force Microscopy. *J Phys Chem B* 2000, **104**(51): 12282-12291.
4. Mogi R, Inaba M, Iriyama Y, Abe T, Ogumi Z. In Situ Atomic Force Microscopy Study on Lithium Deposition on Nickel Substrates at Elevated Temperatures. *J Electrochem Soc* 2002, **149**(4): A385-A390.
5. Orsini F, Du Pasquier A, Beaudoin B, Tarascon JM, Trentin M, Langenhuizen N, *et al.* In situ Scanning Electron Microscopy (SEM) observation of interfaces within plastic lithium batteries. *J Power Sources* 1998, **76**(1): 19-29.
6. Cheng J-H, Assegie AA, Huang C-J, Lin M-H, Tripathi AM, Wang C-C, *et al.* Visualization of Lithium Plating and Stripping via in Operando Transmission X-ray Microscopy. *J Phys Chem C* 2017, **121**(14): 7761-7766.
7. Kushima A, So KP, Su C, Bai P, Kuriyama N, Maebashi T, *et al.* Liquid cell transmission electron microscopy observation of lithium metal growth and dissolution: Root growth, dead lithium and lithium flotsams. *Nano Energy* 2017, **32**: 271-279.
8. Li Y, Li Y, Pei A, Yan K, Sun Y, Wu C-L, *et al.* Atomic structure of sensitive battery materials and interfaces revealed by cryo-electron microscopy. *Science* 2017, **358**(6362): 506-510.
9. Wang X, Zhang M, Alvarado J, Wang S, Sina M, Lu B, *et al.* New Insights on the Structure of Electrochemically Deposited Lithium Metal and Its Solid Electrolyte Interphases via Cryogenic TEM. *Nano Lett* 2017, **17**(12): 7606-7612.
10. Dubrovskii V. Fundamentals of Nucleation Theory. *Nucleation Theory and Growth of Nanostructures*. Springer Berlin Heidelberg: Berlin, Heidelberg, 2014, pp 1-73.

11. Scharifker B, Mostany J. Electrochemical Nucleation and Growth. *Encyclopedia of Electrochemistry*, 2007.
12. Ely DR, Jana A, García RE. Phase field kinetics of lithium electrodeposits. *J Power Sources* 2014, **272**: 581-594.
13. Ely DR, García RE. Heterogeneous Nucleation and Growth of Lithium Electrodeposits on Negative Electrodes. *J Electrochem Soc* 2013, **160**(4): A662-A668.
14. Akolkar R. Modeling dendrite growth during lithium electrodeposition at sub-ambient temperature. *J Power Sources* 2014, **246**: 84-89.
15. Akolkar R. Mathematical model of the dendritic growth during lithium electrodeposition. *J Power Sources* 2013, **232**: 23-28.
16. Chazalviel JN. Electrochemical aspects of the generation of ramified metallic electrodeposits. *Phys Rev A* 1990, **42**(12): 7355-7367.
17. Greer AL. Metallic Glasses. *Science* 1995, **267**(5206): 1947-1953.
18. Wang X, Li Y, Meng YS. Cryogenic Electron Microscopy for Characterizing and Diagnosing Batteries. *Joule* 2018, **2**(11): 2225-2234.
19. Wang F, Graetz J, Moreno MS, Ma C, Wu L, Volkov V, *et al.* Chemical Distribution and Bonding of Lithium in Intercalated Graphite: Identification with Optimized Electron Energy Loss Spectroscopy. *ACS Nano* 2011, **5**(2): 1190-1197.
20. Jafary-Zadeh M, Praveen Kumar G, Branicio P, Seifi M, Lewandowski J, Cui F. A Critical Review on Metallic Glasses as Structural Materials for Cardiovascular Stent Applications. *Journal of Functional Biomaterials* 2018, **9**(1): 19.
21. van Duin ACT, Dasgupta S, Lorant F, Goddard WA. ReaxFF: A Reactive Force Field for Hydrocarbons. *J Phys Chem A* 2001, **105**(41): 9396-9409.
22. Plimpton S, Crozier P, Thompson A. LAMMPS-large-scale atomic/molecular massively parallel simulator. *Sandia National Laboratories* 2007, **18**: 43.
23. Majure DL, Haskins RW, Lee NJ, Ebeling RM, Maier RS, Marsh CP, *et al.* Large-Scale Atomic/Molecular Massively Parallel Simulator (LAMMPS) Simulations of the Effects of Chirality and Diameter on the Pullout Force in a Carbon Nanotube Bundle. 2008 DoD HPCMP Users Group Conference; 2008 14-17 July 2008; 2008. p. 201-207.

24. Stukowski A. Visualization and analysis of atomistic simulation data with OVITO—the Open Visualization Tool. *Modelling and Simulation in Materials Science and Engineering* 2009, **18**(1): 015012.
25. Onofrio N, Strachan A. Voltage equilibration for reactive atomistic simulations of electrochemical processes. *The Journal of Chemical Physics* 2015, **143**(5): 054109.
26. Jensen BD, Wise KE, Odegard GM. The effect of time step, thermostat, and strain rate on ReaxFF simulations of mechanical failure in diamond, graphene, and carbon nanotube. *J Comput Chem* 2015, **36**(21): 1587-1596.
27. Cui Z, Gao F, Cui Z, Qu J. Developing a second nearest-neighbor modified embedded atom method interatomic potential for lithium. *Modelling and Simulation in Materials Science and Engineering* 2011, **20**(1): 015014.
28. Stukowski A. Structure identification methods for atomistic simulations of crystalline materials. *Modelling and Simulation in Materials Science and Engineering* 2012, **20**(4): 045021.
29. Baldan A. Review Progress in Ostwald ripening theories and their applications to nickel-base superalloys Part I: Ostwald ripening theories. *J Mater Sci* 2002, **37**(11): 2171-2202.
30. Nanov CN. Theory of nucleation. *Handbook of Crystal Growth (Second Edition)*. Elsevier, 2015, pp 315-358.
31. Karthika S, Radhakrishnan TK, Kalaichelvi P. A Review of Classical and Nonclassical Nucleation Theories. *Cryst Growth Des* 2016, **16**(11): 6663-6681.
32. Fang C, Wang X, Meng YS. Key Issues Hindering a Practical Lithium-Metal Anode. *Trends in Chemistry* 2019, **1**(2): 152-158.
33. Mehdi BL, Stevens A, Qian J, Park C, Xu W, Henderson WA, *et al.* The Impact of Li Grain Size on Coulombic Efficiency in Li Batteries. 2016, **6**: 34267.
34. Khan MM, Nemati A, Rahman ZU, Shah UH, Asgar H, Haider W. Recent Advancements in Bulk Metallic Glasses and Their Applications: A Review. *Crit Rev Solid State Mater Sci* 2018, **43**(3): 233-268.

35. Lu X, Tjaden B, Bertei A, Li T, Li K, Brett D, *et al.* 3D Characterization of Diffusivities and Its Impact on Mass Flux and Concentration Overpotential in SOFC Anode. *J Electrochem Soc* 2017, **164**(4): F188-F195.
36. Chen M. A brief overview of bulk metallic glasses. *Npg Asia Materials* 2011, **3**: 82.
37. Ling C, Banerjee D, Matsui M. Study of the electrochemical deposition of Mg in the atomic level: Why it prefers the non-dendritic morphology. *Electrochim Acta* 2012, **76**: 270-274.
38. Zhou J, Yang Y, Yang Y, Kim DS, Yuan A, Tian X, *et al.* Capturing Nucleation at 4D Atomic Resolution. *arXiv e-prints*; 2018.

Acknowledgments:

We would like to acknowledge the UC Irvine Materials Research Institute (IMRI) for the use of Cryo-Electron Microscopy Facility and Kratos XPS, funded in part by the National Science Foundation Major Research Instrumentation Program under Grant No. CHE-1338173. We thank Dr. Xiaoqing Pan, Dr. Toshihiro Aoki, Dr. Li Xing and Dr. Jian-Guo Zheng for their assistance with the microscopy. Work at the Molecular Foundry was supported by the Office of Science, Office of Basic Energy Sciences, of the U.S. Department of Energy under Contract No. DE-AC02-05CH11231. The SEM was performed in part at the San Diego Nanotechnology Infrastructure (SDNI), a member of the National Nanotechnology Coordinated Infrastructure, which is supported by the National Science Foundation (Grant ECCS-1542148). We also would like to thank Prof. Adri van Duin of the Pennsylvania State University for providing the ReaxFF parameters used in this work. We appreciate Dr. Wu Xu and Dr. Marco Olguin for discussing the results.

Funding:

This work is supported by the Assistant Secretary for Energy Efficiency and Renewable Energy, Office of Vehicle Technologies of the U.S. Department of Energy in the Advanced Battery Materials Research (BMR) Program (Battery500 Consortium). INL is operated by Battelle Energy Alliance under Contract No. DE-DE-AC07-05ID14517 for the U.S. Department of Energy.

Author Contributions:

XW, SM, and BL conceived the idea. XW designed the experiments and conducted the cryo-TEM. YL, BL, MZ, and AB helped with cell making, electrochemical performance evaluation, EELS and SEM. XW, YL and SM analyzed and discussed the experimental data. XW and YL made the schematic images. GP, ED and BL developed the concept on *r*-MD approach. GP conducted the simulation work. BL provided the major interpretation and discussion of the *r*-MD work in the paper. XR and JZ provided the advanced electrolyte and the anode-free electrochemical performance. PL, JX, JL and ED participated in discussing the results and commenting on the manuscript. The manuscript was mainly written and revised by XW, BL, GP and SM. All authors have given approval to the final version of the manuscript.

Competing interests:

Authors declare no competing interests.

Data and materials availability:

All data is available in the main text or the supplementary materials.

Supplementary Materials:

Materials and Methods

Figures S1-S18

Tables S1-S2

Movies S1-S6